

NUMERICAL INVESTIGATION OF THE EFFECTS OF VOLUME FORCES ON FLAME PROPAGATION CHARACTERISTICS IN A ROTATING PIPE

GONG Zhen^{a,b,c}, LI Benchu^{a,b,c}, TANG Hao^{a,b,c*}

^a College of Energy and Power Engineering, Nanjing University of Aeronautics and Astronautics,
Nanjing, 210016, China

^b Nanjing University of Aeronautics and Astronautics, Aero-engine Thermal Environment and
Structure Key Laboratory of Ministry of Industry and Information Technology, Nanjing 210016,
China

^c Nanjing University of Aeronautics and Astronautics, Jiangsu Province Key Laboratory of Aerospace
Power System, Nanjing 210016, China.

* Corresponding author; E-mail: hao.tang@nuaa.edu.cn

The combustion of fuel under intense volumetric forces has the potential to enhance the velocity of flame propagation. To investigate the influence of volumetric forces on the combustion process and the characteristics of flame propagation within fuel, this research paper conducted a numerical analysis of a two-dimensional rotating pipe subjected to varying volumetric forces. The findings reveal that, within a specific range, an augmentation in volumetric forces progressively elevates both the global and localized speeds of flame propagation. The primary rationale behind the heightened flame propagation speed under intense volumetric forces lies in the fact that the increase in such forces facilitates an enlargement of the interface area between the burned and unburned gases. This, in turn, fortifies the transfer of heat and the chemical reaction rate between the two, effectively shortening the duration of combustion and augmenting the speed of flame propagation. At exceedingly low volumetric forces, the pressure wave generated by combustion in the pipe exerts a certain influence on the speed of flame propagation and the progression of the flame.

Key words: volumetric forces; ultra-compact combustion; flame propagation speed; Rayleigh-Taylor instability;

1. Introduction

In the pursuit of enhanced efficiency, heightened resilience, and diminished emissions, contemporary aviation gas turbine engines have set forth ambitious objectives for their advancement. Among the triad of fundamental constituents within these engines, the combustion chamber assumes a pivotal role as it facilitates the conversion of fossil fuels into kinetic energy, exerting a direct influence on the aircraft's overall performance. Furthermore, it represents a critical component in realizing the aforementioned goals. The utilization of the ultra-compact combustion (UCC) technology, employing the Rich burn-Quick quench-Lean burn (RQL) combustion organizational methodology, possesses the remarkable capability of considerably curtailing the combustion duration of the fuel. Consequently,

this results in a reduction in the length of the combustion chamber and a consequential augmentation in the thrust-to-weight ratio of the gas turbine[1-3].

High-G-loading Combustion (HGC) stands as a pivotal technological in attaining High-G UCC. It entails the application of a combustion methodology whereby the fuel undergoes combustion within a designated volume force field, thereby yielding heightened combustion efficacy and accelerated flame propagation velocity. The requisite volume force, denoted as g_0 , typically ranges from 500 to 3000 times the gravitational field, with its magnitude commonly expressed as a ratio relative to the gravitational acceleration. In the context of rotating combustion devices and swirling combustion chambers, the volumetric force g_0 can be defined as $g_0 = u^2/r$. Due to the distinctive attributes of HGC, integrating this approach into aviation engines can amplify the combustion rate of flames within the combustion chamber. This, in turn, leads to the reduction of the axial length of aviation engines and consequently enhances the thrust-to-weight ratio of the engines.

The phenomenon of accelerating flame combustion through high-G-loading was initially observed by Lewis [4] during his experiments involving rotating tube combustion. To elucidate this phenomenon, Lewis put forth the Buoyant Bubble Transport Mechanism[5, 6], which posits that the flame propagation velocity is governed by both the turbulent flame propagation mechanism and the bubble transport velocity generated. The greater value between the two determines the flame propagation velocity. When the volumetric force is low, the bubble transport velocity remains inferior to the turbulent flame propagation velocity, resulting in the flame propagation being controlled by the turbulent flame mechanism. However, as the volumetric force increases, the disparity in acceleration between the flame front and the surrounding gas gradually amplifies, leading to a corresponding increase in the bubble transport velocity. Eventually, the bubble transport velocity surpasses the turbulent flame propagation velocity. At this juncture, the flame propagation becomes governed by the bubble transport mechanism, and augmenting the volumetric force yields an elevation in the flame propagation velocity. Nevertheless, as the volumetric force continues to rise, the excessive bubble transport velocity induces greater heat dissipation within the moving flame front, resulting in a partial quenching of the flame and, ultimately, a steep decline in the flame propagation velocity.

Katta et al. [7] simplified Lewis' experiment by developing a two-dimensional model that considered an infinitely long direction for flame propagation. They employed direct numerical simulations to replicate the combustion process of hydrogen-air premixed gases with within volume force fields of 10g and 500g. The obtained simulation results closely resembled Lewis' experimental findings, thereby further substantiating the theory of gas bubble transport. Yukio Sakai et al. [8] carried out experimental studies on flame propagation in a rigid rotating flow field. The gases were filled in open-ended pipes, where the rotation center coincided with the axis of the pipe. The experiments revealed that as the rotational speed of the pipe increased, the flame propagation speed at specific locations within the pipe demonstrated a nearly linear growth. Additionally, the introduction of volume force expanded the combustion limit of the premixed fuel, allowing for sustained combustion under these conditions. Briones et al. [9] employed a model that closely resembled Lewis's experiment, utilizing a closed, X-axis symmetric two-dimensional model to numerically simulate the combustion within a rotating reference frame. The simulation results concurred with Lewis's experimental findings and highlighted the combined effects of density disparity between the burned and unburned gases and the centrifugal force, which fostered the occurrence of Rayleigh-Taylor (R-T) instability. This instability, coupled with the flame speed resulting from thermal expansion and

turbulence, constituted the mechanism for flame propagation towards the opposite end, consequently accelerating the flame propagation speed to some extent under the influence of R-T instability. Liu et al.[10] expanded upon Briones's work by introducing a turbulence generator into the model. They considered the effect of Coriolis force and centrifugal force on the flame propagation speed in a closed pipe. It was observed that in a closed rotating combustion system, Coriolis force also exerted a certain influence on the flame propagation speed, warranting its consideration alongside other factors.

Although Iuyu et al. and Briones et al. have conducted simulations similar to Lewis's experiments, their combustion conditions were limited to stoichiometric ratios. However, the optimal combustion mode for ultra-compact combustion chambers is the RQL burn strategy. Therefore, studying the combustion characteristics of fuel-air mixtures at different equivalence ratios in high-volume force fields is more relevant to the actual combustion process of ultra-compact combustion. In light of this, the present study aims to numerically investigate propane-air and kerosene-air mixtures at various equivalence ratios under different volume force conditions, with the goal of providing valuable insights for the design of ultra-compact combustion chambers.

2. Computational Model and Methods

2.1. Geometric Model

In order to facilitate a meaningful comparison between the computational results and experimental data available in the literature, the geometric model employed in this study is based on the original Lewis experimental model, which has been simplified to a 2D rectangle. Fig.1 provides a schematic diagram of this geometric model, which encompasses the following key elements: **Turbulence generator:** Positioned 60 mm from the left side, there are fifteen rectangular holes with dimensions of 2 mm \times 2 mm. These holes are strategically placed to act as turbulence generators within the system. **Monitoring surfaces:** Located at a distance of 165 mm from the left side, a series of eight monitoring surfaces are positioned, numbered 1 to 8 from left to right. The spacing between adjacent monitoring surfaces is 50 mm. **Ignition area:** The ignition region is situated on the leftmost side and is delineated by a rectangular area measuring 67mm in length and 5mm in width. The temperature within this region is prescribed to be 2000K. **Rotation center:** The rotation center is situated at the center of the model, with the rotation axis perpendicular to the plane of the paper. The rotational effect is simulated by incorporating source terms in the momentum and enthalpy equations.

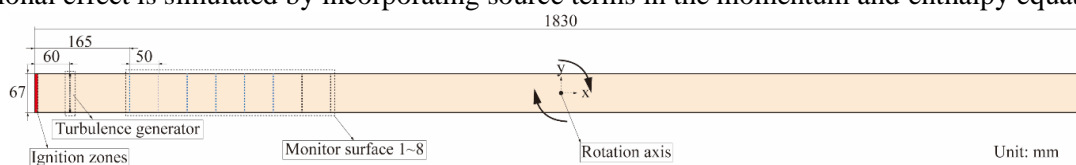


Fig.1 The schematic diagram of the geometric model

2.2. Numerical methods

This article utilizes the commercial software ANSYS Fluent to conduct a range of calculations, known for its high performance in terms of stability and accuracy. The software effectively solves the continuity equation, momentum equation, turbulence kinetic energy equation, turbulence dissipation rate equation, enthalpy equation, and species transport equation[11]. The turbulence model adopted in this study is the self-adaptive (SAS) model, with the coupled scheme utilized for pressure-velocity

coupling. Bounded Second Order Implicit is employed for time discretization, the PRESTO! scheme is applied for pressure discretization, and Least Squares Cell Based is utilized for gradient computation. The second-order Bounded Central Differencing scheme is employed for both the momentum equation and the species transport equation, offering reduced numerical dissipation and better compatibility with SAS and LES turbulence models. The QUICK scheme is employed for density, turbulent kinetic energy, and energy calculations. The ANSYS ICEM software was employed to create a structured grid with a uniform distribution in both the x and y directions, utilizing a grid size of 0.5mm. To accurately capture the high-gradient variations near the walls and ensure a wall Y^+ value below 1, 20 layers of boundary layer mesh were added to all walls. The final mesh consisted of approximately 600,000 nodes. A 2D transient model is employed for the calculation process, with the time step chosen based on the CFL criterion to ensure that the maximum Courant number remains below 1 throughout the simulation. The final time step in this study was determined to be 10^{-6} s. To enhance computational efficiency, this study utilized the Propane-Air-2step and Kerosene-Air global reaction mechanisms[9, 11].

2.3. Initial State and Boundary Conditions

In this paper, the computational model uses adiabatic no-slip wall boundary conditions for all walls. The initial values assigned to temperature, turbulent kinetic energy, and specific dissipation rate as 300 K, 10 [m²s⁻²], and 1 [s⁻¹], respectively. The flame propagation velocity is determined by monitoring eight surfaces set within the computational domain. A user-defined function is employed to record the maximum temperature at each monitoring surface at the end of each time step. If the maximum temperature exceeds 2000 K, it is considered that the flame has propagated to that location, and the corresponding calculation time is outputted. The local flame propagation velocity can be calculated by analyzing the coordinate difference and time difference between adjacent monitoring surfaces. The global flame speed is calculated based on the coordinate difference and time difference between monitoring surface 8 and monitoring surface 4.

2.4. Comparison of the computaiona results with the experimental results

The research findings of Liu et al.[10] indicate that the Coriolis force generated in a closed rotating combustion system cannot be neglected. However, most practical combustion devices are open systems. Hence, in this paper, both centrifugal force and Coriolis force were considered when comparing with experimental values. However, in the formal calculations, only the centrifugal force generated by rotation was considered, and the added source term was $-\rho(\omega \times (\omega \times r))$. The numerical results of this paper are compared with the experimental findings of Lewis et al.[4], as depicted in Fig.2. The G-Loading in Figure 2 represents a dimensionless quantity of the ratio between volume force and gravity.

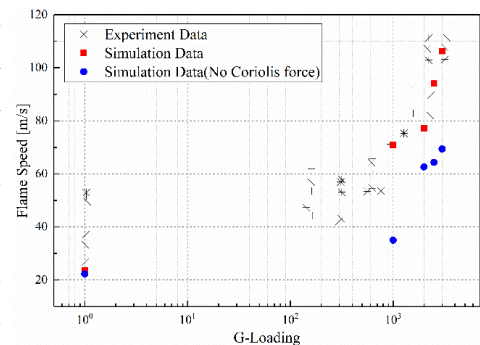


Fig.2 Comparison of Calculation Results and Experimental Results

From the figure, it can be observed that the calculated flame propagation speed exhibits a similar trend to the experimental results as the volume force increases. The calculated values generally

fall within the range of experimental errors. However, for the case of a volume force of 1g, the calculated results are slightly lower than the experimental values. This difference can be attributed to the following reasons: Firstly, the utilization of a two-dimensional model in this study may possess inherent limitations in comprehending the intricacies of turbulence. Secondly, the incorporation of a global reaction mechanism in this investigation inadvertently disregards specific intricacies associated with the reaction process. Upon eliminating the source term associated with the Coriolis force, a substantial reduction in the flame propagation velocity was observed under identical volume force conditions. It is important to note that although the Coriolis force can have a significant impact on flame propagation speed in a closed rotating system, it can be ignored in the calculations for an open combustion system, such as a gas turbine's combustion chamber, where there is no Coriolis force. Hence, the subsequent analysis will disregard the Coriolis force.

3. Results and Discussion

3.1. Influence of Extremely Low and High Volume Forces on Flame Propagation Morphology

The temperature distribution contours at various time intervals for a propane-air mixture with an equivalence ratio of 1.0 under volume forces of 1g and 2500g are depicted in Fig.3 and 4, respectively. The red curve on the right side represents the flame front at the corresponding time. Fig.5 illustrates the temperature and pressure gradient distributions at different times under a volume force of 1g. To enhance the clarity of the propagation process of the flame and pressure waves inside the tube, the temperature and pressure wave data were normalized in this study. It should be noted that the numerical values on the Y-axis only represent offset values and do not reflect actual magnitudes.

According to Fig.3, initially, the C_3H_8 -air mixture contained in the pipe undergoes rapid ignition due to the high-temperature ignition zone located on the left side. This ignition event leads to a sudden expansion and density decrease in that region, resulting in a sudden pressure change inside the pipe and the formation of a strong pressure wave propagating towards the right side. Subsequently, under the influence of thermal expansion, the high-temperature region gradually expands towards the right side, inducing Darrieus-Landau instability. This instability leads to the gradual formation of a wavy flame front (at 4 ms). At the 12 ms mark, as the flame progresses, it undergoes a transformation from a wavy configuration to a wrinkled structure, and the central protrusion shifts from a single peak to a double peak. This alteration in morphology can be attributed to the following factors: Referring to Fig.5, the strong pressure wave generated during ignition rebounds off the right wall and traverses through the turbulence generator, subsequently encountering the flame front for the first time around the 10ms mark. Due to the nearly planar nature of the pressure wave, its primary interaction occurs with the central protrusion of the flame front towards the right, leading to a partial impediment of the flame's propagation in that particular direction. Consequently, the flame front undergoes a transition from a single peak to a double peak morphology at the 12 ms interval. As time progresses, the flame traverses the turbulence generator, resulting in the formation of multiple fragmented flames (at 16 ms). Subsequently, these fragmented flames quickly merge together and propagate rapidly in the unburned direction, gradually assuming a finger-like flame structure (at 20 ms, indicated by the red arrow).

As the flame progresses, the finger-like flame front gradually dissipates, supplanted by a flame front evocative of a tulip shape positioned at the leading edge of the flame (at 24 ms). Moreover, one can observe that the leading edge of the flame is connected to the high-temperature region on the left

via a slender "neck" area (indicated by the green arrow). During this process, the flame front undergoes a repeated transition from a single-peak morphology to a double-peak morphology. In comparison to the initial occurrence, the double-peak morphology is more prominent, characterized by higher peak values and a longer duration. The reason for the observed flame front morphology can be explained as follows: In Fig.5, it is observed that the strong pressure wave, after undergoing multiple reflections from the walls, encounters and interacts with the flame front again at 20.3 ms. Moreover, prior to the interaction, the flame front exhibits a more prominent protrusion at the leading edge, and there is a greater accumulation of unburned gas near the wall at 20 ms. Consequently, the interaction between the nearly planar pressure wave and the protruding flame front becomes more pronounced. The pressure wave instantaneously compresses the flame at the center of the pipe in the direction of the burned region (left and upper/lower sides), leading to the longitudinal propagation of the flame front along the upper and lower wall directions. Following the passage of the strong pressure wave, the flames near the upper and lower walls continue propagating towards the right, while the flame at the center, influenced by inertia, maintains a concave shape towards the left.

As the flame continues to propagate towards the right, the tulip-shaped flame gradually diminishes and transforms into a crescent-shaped flame front at 26 ms. It is important to note that during the time interval from 24 ms to 26 ms, the flame propagates only a very short distance towards the right, and there is even a leftward movement near the central region of the pipe (indicated by the purple arrow). This phenomenon can be explained as follows: Referring to Fig.5, behind the strong pressure wave, there are multiple weak pressure wave packets. Although they possess lower intensity compared to the strong pressure wave, they have a longer interaction time. Consequently, they incessantly engage with the advancing flame front, exerting an influence on its configuration and inducing a discernible leftward displacement. Subsequently, the flame continued its propagation towards the unburned direction, while the protruding portion near the wall gradually approached the center. At 32 ms, the flame front once again assumed a double-peak shape, possibly due to the third interaction between the flame front and the strong pressure wave.

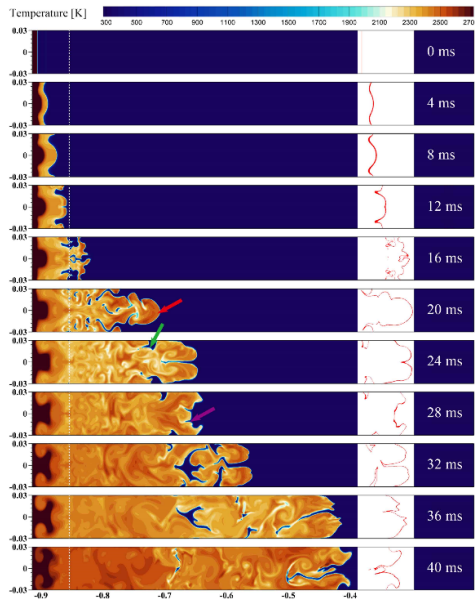


Fig.3 The temperature distribution contours under volume forces of 1g

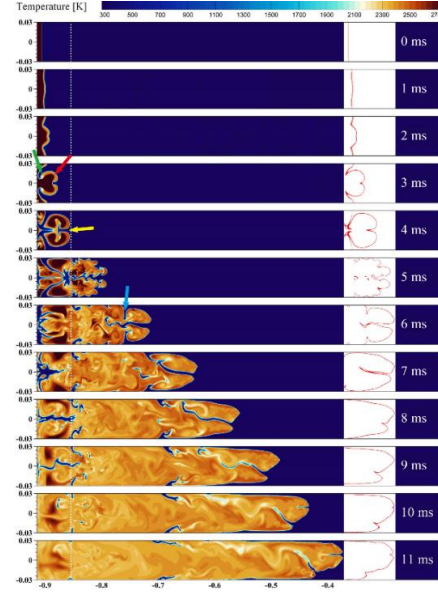


Fig.4 The temperature distribution contours under volume forces of 2500g

The Fig.4 reveals that the mixed gas is ignited, and at the 1ms mark, the flame surface exhibits minor perturbations that quickly escalate. At 3 ms, the high-temperature region and the low-

temperature region display bubble-like structures (highlighted by the red arrow) and finger-like structures (highlighted by the green arrow), respectively. By 4 ms, the high-temperature region takes on a shape reminiscent of a mushroom cloud (indicated by the yellow arrow). The aforementioned phenomena can be attributed to the following factors: Upon ignition by the high-temperature region at the left side of the pipeline, the density of the gas mixture undergoes a rapid decrease, leading to a significant density difference between the unburned and burned gases. This density disparity, coupled with the influence of the intense volume force, causes the unburned gas to be propelled towards both ends of the pipeline, thereby initiating the R-T instability between the unburned and burned gases. During the period between 0 and 1 ms, small disturbances emerged at the interface between the unburned and burned gases, characterized by an amplitude smaller than the wavelength. This phase represents the linear growth stage of the R-T instability. Subsequently, from 1 to 2 ms, the disturbance amplitude gradually increased, approaching the wavelength and entering the nonlinear growth stage of the R-T instability. As time progressed, the disturbances rapidly underwent nonlinear growth. By 3 ms, the distinct bubble and spike structures characteristic of the R-T instability were formed. The mushroom-shaped cloud observed in the high-temperature region can be attributed to the Kelvin-Helmholtz instability, which occurs when the bubble and spike structures arise at the interface between the unburned and burned gases, exhibiting different motion directions.

In comparison to the flame front formed under a volume force of $1g$, the presence of a distinct "neck" (indicated by the light blue arrow) connecting to the left-side high-temperature region becomes more pronounced under a volume force of $2500g$. Furthermore, notable irregular low-temperature regions can be observed within the left-side high-temperature area under the higher volume force, likely resulting from the increased involvement of unburned gas influenced by the R-T instability. When comparing the shape of the flame front, it becomes evident that the flame front under the $2500g$ volume force appears more rounded. As the flame propagates towards monitoring plane 8 (at x-coordinate -0.4), the flame front primarily takes on a bimodal shape. Notably, unlike the scenario involving a $1g$, the strong pressure wave has yet to interact with the flame front during this process. Consequently, the occurrence of this bimodal shape can be attributed to the R-T instability.

3.2. Influence of Extremely Low and High Volume Forces on Flame Propagation Morphology

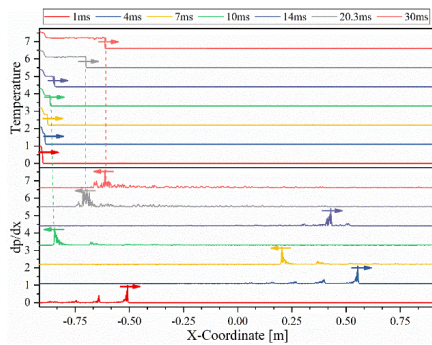


Fig 5. Distribution of temperature and pressure gradients under $1g$ volume force

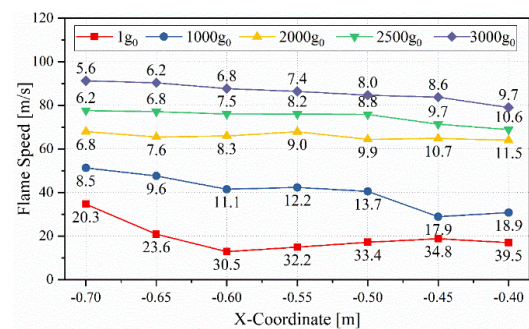


Fig 6. Variation curves of local flame propagation velocity under different volume forces

As a result of the varying centrifugal forces produced by different rotating radii under the identical angular velocity, the volume force acting upon the flame diminishes gradually as it propagates from the left side of the pipe towards the center. This study computed the localized flame propagation speed at monitoring surfaces 2 to 8 (X-axis coordinate position $[-0.7, -0.4]$) under different volume forces, and the corresponding variation curve is depicted in Fig.6.

By analyzing the depicted graph, it becomes apparent that as the flame advances towards the rotational center (X-axis coordinates ranging from -0.70 to -0.40), the local flame propagation velocity experiences a gradual decline under the volume forces of 2000g, 2500g, and 3000g. Conversely, under the volume forces of 1000g and 1g, the flame propagation velocity displays an initial decrease followed by a subsequent gradual increase. This behavior can be attributed to the diminishing volume forces exerted on the flame as it progresses towards the center of rotation, resulting in a reduction in the flame propagation velocity. Furthermore, the combustion of gas situated on the left side of the flame front induces rapid expansion and a concurrent elevation in pressure within the pipe, which further contributes to the diminishment of the flame propagation velocity. As previously mentioned, the flame in the pipe propagation process is also influenced by pressure waves. When subjected to higher volume forces, the flame exhibits an accelerated propagation, reaching the monitoring surface 8 (X-coordinate -0.40) before the pressure wave has sufficient time to interact with the flame front. As a consequence, the impact of the pressure wave on the flame propagation velocity is minimal. Conversely, under lower volume forces, the flame front encounters the pressure wave and undergoes interaction prior to reaching the monitoring surface 8. This interaction momentarily diminishes the flame propagation velocity. However, following the interaction, the flame propagation velocity gradually increases. Hence, under the volume forces of 1000g and 1g, the combined effects of pressure waves, diminishing volume forces within the pipe, and augmented pressure within the pipe collectively contribute to the observed pattern of initially decreasing and subsequently increasing flame propagation velocity. To further investigate the influence of volume forces on flame propagation, this study scrutinized the temporal variation of flame area for each volume force during the computational process. To facilitate subsequent comparisons with the ensuing discussion on kerosene-air fuel, the flame area was determined by calculating the area enclosed between temperature values of 2000 K and 2200 K. While this method may not accurately capture the instantaneous flame area, it effectively portrays the trend of flame area variation over time. The corresponding variation curves are illustrated in Figure 7.

From the observations in Fig.7, it is evident that prior to 2 ms, the flame surface area remains approximately constant at around $0.07 \times 10^{-4} \text{ m}^2$ across all volume forces. Subsequently, under volume forces exceeding 1000g (referred to as higher volume forces), the flame area experiences a rapid and time-dependent increase, with the rate of increase becoming more pronounced as the volume force escalates. However, in the case of 1g volume force, this value remains constant until approximately 10 ms. The underlying factors contributing to this observed trend in flame surface area under higher volume forces can be elucidated as follows: As elucidated earlier, higher volume forces swiftly instigate R-T instability between the burned gas and unburned gas. Based on the investigations carried out by Youngs [12], it has been established that the penetration depth (h_I) resulting from the development of R-T instability is connected to the Atwood number (A) and the volume force (g_0). Mathematically, this relationship can be expressed as: $h_I = \beta A g_0 t^2$. Considering the relatively minor fluctuation in the Atwood number throughout the combustion process investigated in this study, it can be inferred that, at a given point in time, the penetration depth resulting from R-T instability is roughly positively correlated with the volume force. Consequently, during the developmental phase, a higher volume force contributes to a more rapid augmentation in the flame surface area.

Under higher volume forces, the flame area demonstrates localized fluctuations after reaching a value of approximately $1 \times 10^{-4} \text{ m}^2$. By examining the temperature cloud maps at various time points, it

becomes apparent that these fluctuations in flame area correspond to the moment when the flame passes through the turbulence generator. This suggests that beyond the point of traversing the turbulence generator, further increments in the volume force beyond 1000g have minimal influence on the final flame area, although they can enhance the growth rate of the flame area. Consequently, subsequent interactions between the combustion flame and the wall lead to fragmentation-merger phenomena and localized quenching, resulting in localized fluctuations in the flame area. In contrast, under 1g and 1000g volume forces, the flame area exhibits global fluctuations. Through a comprehensive analysis of Figure 7, coupled with the examination of pressure waves within the pipe, it can be inferred that these fluctuations are primarily caused by the interaction between pressure waves and the flame front. Based on the aforementioned analysis, the following conclusions can be drawn: increasing the volume force enhances the contact area between the burned and unburned gases, thereby intensifying heat transfer and accelerating chemical reaction rates. This leads to a shortened combustion time and an overall increase in the flame propagation speed.

During the combustion process, the expansion of burned gas and the occurrence of gas flow due to R-T instability under heightened volume forces engender a localized flow velocity, denoted as U_{flow} , within the pipe. Hence, the previously measured flame propagation speed, U_f , encompasses both the turbulent flame speed, U_t , and the localized flow velocity, U_{flow} , denoted as $U_f = U_t + U_{flow}$. In order to delve deeper into the factors contributing to the amplified flame propagation speed resulting from increased volume forces, the methodology outlined in reference [9] was employed to calculate the turbulent flame speed. The fluctuation of the turbulent flame speed, calculated employing the aforementioned methodology over the course of time, is delineated in Fig.8.

Upon careful examination of the graph, it becomes apparent that the U_t demonstrates a similar variation trend across the higher volume forces. The maximum speed attained during this process reaches approximately 8 m/s. However, in the case of the 1000g volume force, the turbulent flame speed displays two distinct rapid increases. Upon careful analysis of the temperature contour maps at various time intervals, it can be inferred that the initial rapid increase in turbulent flame speed observed in the higher volume forces aligns with the moment when the flame traverses the turbulence generator. Hence, this can be attributed to the influence exerted by the flame passing through the turbulence generator. The second surge in turbulent flame speed observed in the 1000g scenario emerges as a result of the interplay between the flame and pressure waves. Under the 1g volume force, a similar trend is observed. Therefore, it is evident that the fluctuations in turbulent flame speed within the pipe primarily result from the interaction between the turbulence generator and pressure waves. While increasing the volume force can expedite the rising trend of turbulent flame speed, it does not significantly enhance the overall global propagation speed of the turbulent flame. This further underscores that the increased flame propagation speed under larger volume forces primarily stems from the augmented thermal expansion of the burned region and the intensified R-T instability.

3.3. Influence of Fuel on Flame Propagation Characteristics under High Volume Forces

In practical applications of ultra-compact combustion devices, the utilization of high volume forces is imperative to minimize the weight ratio occupied by the combustion chamber. In aviation engines, aviation kerosene stands as the preferred fuel. Hence, the present study undertook simulations to explore the impacts of Kerosene-air premixed fuel under conditions of elevated volume forces.

Specifically, the temperature distribution contours was examined for Kerosene-air, with an equivalence ratio of 1.0 and a volume force of 2500g, as illustrated in Fig.9.

Upon comparing Fig.9 with Fig.4 and conducting a thorough analysis of the results, it becomes apparent that the transition from C_3H_8 fuel to a Kerosene-air mixture, under identical volume force conditions, does not yield a significant alteration in the evolving shape of the temperature field at different time intervals. Notably, the "neck" region, which connects the leading section of the flame with the high-temperature area on the left side, becomes narrower and more elongated. The flame front manifests a conspicuously accentuated bimodal configuration with heightened peak magnitudes. Furthermore, the symmetry of the high-temperature region about the central axis becomes more distinct, persisting until approximately 10 ms before gradually dissipating.

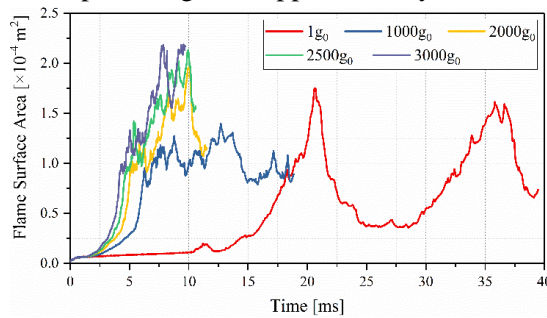


Fig7. Curves of flame surface variation under different volumetric forces

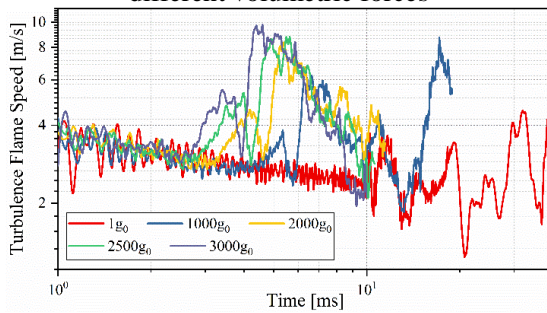


Fig 8. Curves of turbulent flame speed variation

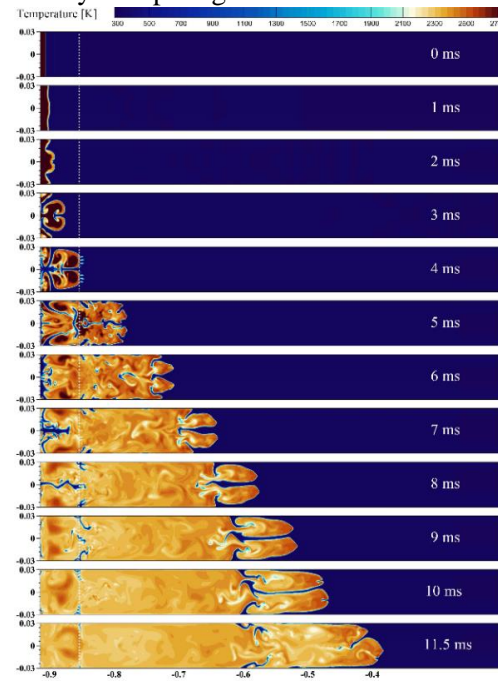


Fig.9 The temperature distribution for Kerosene-air

These observed distinctions can be attributed to the following factors: Kerosene possesses a higher molecular weight compared to C_3H_8 , leading to a greater density disparity between the burned and unburned gases. Consequently, this results in a deeper penetration depth prompted by R-T instability, which contributes to the accentuated bimodal shape of the flame front. Figure 10 depicts the flame area variation with combustion time for Kerosene and C_3H_8 fuels, both operating at a volume force of 2500g and an equivalence ratio of 1.0.

Analyzing the figure reveals a similar trend in the flame area variation curves for both fuels. Initially, as time progresses, the flame area experiences growth, followed by a subsequent decrease occurring around 9.5 ms for both fuels. This indicates that the effect of volume force on the change in flame area is relatively similar for these two fuels. However, in terms of magnitude, the flame area for Kerosene-air fuel surpasses that of C_3H_8 -air at the same time interval. This further reinforces the notion that R-T instability exerts a more substantial influence on fuels with higher molecular weights.

3.4. Effect of equivalent ratio on flame propagation characteristics under high volume force

To examine the impact of equivalence ratio on flame propagation characteristics under high volume forces, this study conducted numerical simulations of C_3H_8 and Kerosene fuels at various

equivalence ratios, while maintaining a volume force of 3000g. Although the employed global reaction mechanism may not capture the intricate details of lean and rich combustion, it provides a general understanding of the effects of different equivalence ratios on combustion characteristics. Fig.10 showcases the variation of global flame propagation speed with equivalence ratio for C_3H_8 and Kerosene fuels under the specified volume force.

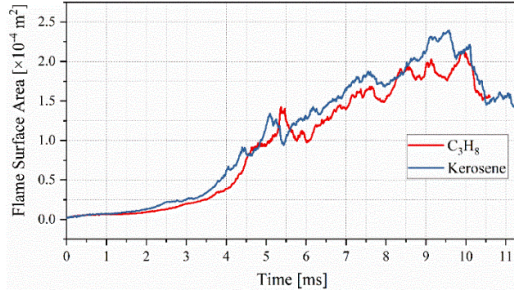


Fig 10. Variation of flame area with combustion time for Kerosene and C_3H_8 fuels

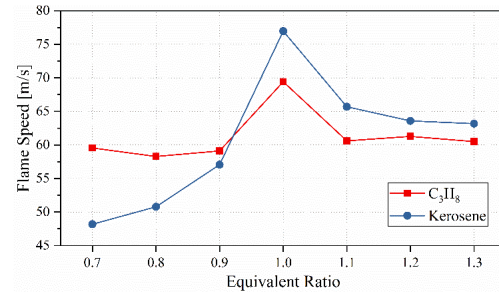
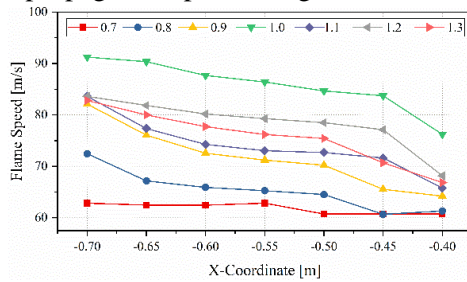
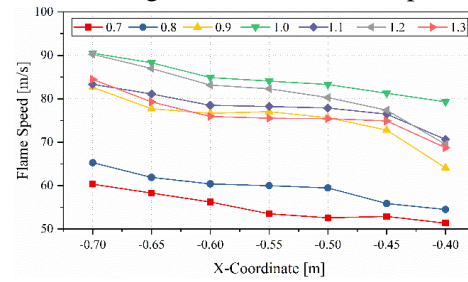


Fig 11. Variation curves of global flame propagation speed with equivalence ratio

Upon analyzing the figure, it becomes apparent that both fuels exhibit a similar pattern of initially increasing and subsequently decreasing global flame propagation speed as the equivalence ratio increases. The peak speed is achieved at an equivalence ratio of 1.0 for both fuels. Since the Lewis number (Le) was kept constant throughout the simulation, the primary cause of the observed variations is the alteration in combustion temperature that results from changes in equivalence ratio. This change, in turn, leads to variations in flame propagation speed. Notably, the influence of equivalence ratio is more prominent for lean mixtures (equivalence ratio < 1) compared to rich mixtures (equivalence ratio > 1), aligning with the behavior of laminar premixed flames. Furthermore, it can be observed that the effect of equivalence ratio on the global flame propagation speed is more pronounced for Kerosene fuel in comparison to C_3H_8 fuel. Fig.12 illustrates the fluctuations in local flame propagation speed along the x-coordinate for both fuels throughout the combustion process.



(a) C_3H_8



(b) Kerosene

Fig 12. Variation curves of local flame propagation velocity

From the graphical representations, it is apparent that the local flame velocities of both fuels decrease gradually as the x-coordinate increases. This trend can be attributed to the gradual reduction in the applied volume force. Thus, it can be concluded that high volume force affects the flame propagation velocity in a similar manner for different fuel equivalence ratios. Additionally, it is noteworthy that Kerosene exhibits relatively higher local flame propagation velocities, and the variation curve of velocities is more concentrated within the equivalence ratio range of 0.9 to 1.3.

4. Conclusion

Numerical calculations were carried out in this study to examine the combustion process of various fuels in a closed rotating duct. The study investigated the impact of different volume forces, fuels, and equivalence ratios on flame propagation characteristics. The findings suggest that:

(1) Under extremely low volume forces, the combustion process undergoes a notable transition between single-peaked and double-peaked flame configurations. Furthermore, the flame front interacts with pressure waves multiple times. The strong pressure wave contribute to a moderate expansion of the flame area, whereas the pressure wave packets can impede the flame propagation speed.

(2) Within a specified range, the flame propagation velocity exhibits a gradual augmentation as the volume force increases. The heightened volume force fosters an enlarged contact area between the combusted and unburned gases, effectively facilitating heat transfer and elevating chemical reaction rates. This, in turn, leads to a reduction in the combustion time and ultimately amplifies the flame propagation velocity.

(3) The augmented flame propagation speed under higher volume forces can be primarily attributed to the increased thermal expansion of the combusted region and the heightened Rayleigh-Taylor instability, which enhances the mixing and combustion processes.

(4) The impact of volume force on the characteristics of C_3H_8 and Kerosene fuels displays a general similarity. However, it is noteworthy that the equivalence ratio exerts a more significant influence on Kerosene compared to C_3H_8 .

Acknowledgment

This research is supported by the National Natural Science Foundation of China (NSFC 51076064 and NSFC No. 91641131) and the Fundamental Research Funds for the Central Universities (NO. NP2022102).

References

- [1] Peterson, C.O., *et al.*, Performance of a model rich burn-quick mix-lean burn combustor at elevated temperature and pressure, 'Report, 2002.
- [2] Straub, D.L., *et al.*, Assessment of rich-burn, quick-mix, lean-burn trapped vortex combustor for stationary gas turbines, *J. Eng. Gas Turbines Power*, 127. (2005), 1, pp. 36-41
- [3] Meziane, S.,A. Bentebbiche, Numerical study of blended fuel natural gas-hydrogen combustion in rich/quench/lean combustor of a micro gas turbine, *International Journal of Hydrogen Energy*, 44. (2019), 29, pp. 15610-15621
- [4] Lewis, G.D., Combustion in a centrifugal-force field, *Symposium (International) on Combustion*, 13. (1971), 1, pp. 625-629, DOI No. [https://doi.org/10.1016/S0082-0784\(71\)80064-4](https://doi.org/10.1016/S0082-0784(71)80064-4)
- [5] Lewis, G.D. *Centrifugal-force effects on combustion*,Symposium (International) on Combustion,1973,14, pp. 413-419
- [6] Lewis, G.D., *et al.*, Swirling Flow Combustion, *Journal of Energy*, 1. (1977), 4, pp. 201-205, DOI No. 10.2514/3.62330
- [7] Katta, V., *et al.*, *Effect of Centrifugal Forces on Flame Stability in an Ultra-Compact Combustor*, 51st AIAA Aerospace Sciences Meeting including the New Horizons Forum and Aerospace Exposition. 2013.
- [8] Sakai, Y.,S. Ishiuka. *The phenomena of flame propagation in a rotating tube*,Symposium (International) on combustion,1996,26, pp. 847-853
- [9] Briones, A.M., *et al.*, Effect of Centrifugal Force on Turbulent Premixed Flames, *Journal of Engineering for Gas Turbines and Power*, 137. (2015), 1
- [10] Liu, Y., *et al.*, Numerical Investigation of Turbulent Premixed Combustion in a High Acceleration Field, *Journal of Thermal Science and Engineering Applications*, 12. (2020), 4, p. 041010
- [11] ANSYS, A.F.R., *Ansys Fluent Theory Guide*. Canonsburg, 2021.
- [12] Youngs, D.L., Numerical simulation of turbulent mixing by Rayleigh-Taylor instability, *Physica D: Nonlinear Phenomena*. (1984),

Submitted: 04.06.2023.
Revised: 17.08.2023.
Accepted: 22.08.2023.